THE JOURNAL OF PHYSICAL CHEMISTRY C
A JOURNAL OF THE AMERICAN CHEMICAL SOCIETY

pubs.acs.org/JPCC

Article

Electronic and Optical Properties of Sn/Ge-Substituted 2D Dion-Jacobson Phase $(3\text{-AMPY})_4Pb_4I_{16}$ Perovskite for Photovoltaic Applications: A First Principle Study

Frew Gashaw Asefa, Aseres Alula Arega, Getachew Gizaw Kebede, Yedilfana Setarge Mekonnen,* and Kingsley Onyebuchi Obodo*

Cite This: *J. Phys. Chem. C* 2024, 128, 14158−14167

Read Online

ACCESS | Metrics & More | Article Recommendations | Supporting Information

ABSTRACT: The structural, electronic, optical, and photovoltaic properties of Sn/Ge-substituted 2D slightly shifted DJ phase $(3\text{-AMPY})_4Pb_4I_{16}$ perovskite were investigated using first principle calculations. The toxic Pb was substituted in the primary geometry by less toxic Sn/Ge. We found that Ge/Sn doping is energetically favorable for decreasing and eliminating the Pb content in pristine $(3\text{-AMPY})_4Pb_4I_{16}$. On both Ge/Sn doping critical characteristics for perovskite, strong optical absorption, p−p/s-p couplings, and direct band gap are observed. The strong p−p/s-p couplings in both Ge/Sn-substituted conformers decrease the band gap of the pristine $(3\text{-AMPY})_4Pb_4I_{16}$ to the value suitable for photovoltaic applications. This further helps us get good optical absorption coefficient and high-power conversion efficiency in $(3\text{-AMPY})_4Pb_{4-x}Ge_xI_{16}$ (x = 1, 2, 3, 4) and $(3\text{-AMPY})_4Ge_{4-x}Sn_xI_{16}$ conformers. The partial density of states and band structure plots show significant contributions of the dominant organic cation to the conduction band minimum. This contribution becomes more pronounced with increasing Ge/Sn doping. The presence of Ge/Sn dopant atoms in the substituted 2D $(3\text{-AMPY})_4Pb_4I_{16}$ perovskite showed improved photovoltaic performance compared to that of the pristine system. This study should form a basis for realizing a more benign photovoltaic perovskite-based system.

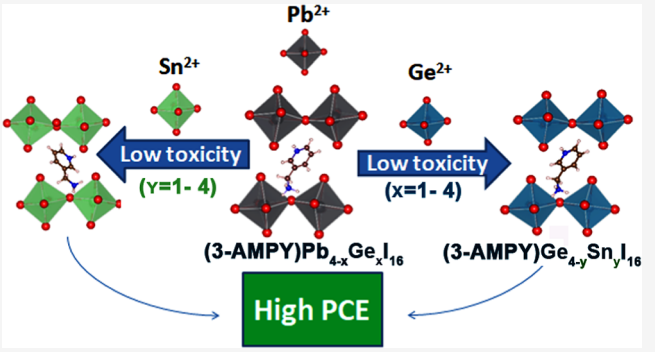

1. INTRODUCTION

The exploration of stable and nontoxic perovskite systems for photovoltaic applications continues unabated.[1−3] Perovskite materials show potential for use in solar applications due to their impressive optical and electronic characteristics, such as high absorption, adjustable band gap, and good carrier mobility.[4−6] Recent studies have achieved a high-power conversion efficiency (PCE) of over 25% using hybrid organic−inorganic perovskite (OIHP) sensitizers, surpassing silicon sensitizers.[7]

Some of the advantages of OIHPs include being lightweight, flexibility, and their low processing cost compared with commercial silicon-based solar cells.[8−10] However, despite the advancements in increasing PCE and reducing processing costs, the widespread commercialization of perovskite solar cells is hindered by long-term stability issues[11,12] and concerns regarding lead (Pb) toxicity.[13,14] Research has found that two-dimensional Dion-Jacobson (DJ) phase perovskites offer better stability than 3D and other 2D phases.[15−17] However, the increased stability can lead to lower device performance due to inefficient charge transfer between layers and a larger quantum well from dimensional reduction and the size of organic cations. Recent studies have investigated the use of short aromatic piperidinium cations, like 3-(aminomethyl) pyridinium (3-AMPY), to address these issues and enhance efficiency compared to other organic spacers.[18]

Doping of Pb by Sn/Ge has been studied and revealed that Sn and Ge are a potential substitute for toxic Pb in perovskite geometry.[19,20] Investigating various optoelectronics applications in 2D DJ phase perovskite is an up-to-date research interest.[1,21,22] However, no sufficient literature data exist on doping of 2D DJ phase with Ge/Sn and their respective impacts on structural, electronic, optical, and photovoltaic performance properties. $(3\text{-AMPY})_4$ Pb_4I_{16} shows a direct band gap of 2.34 and PCE of 9.2%.[18] Compared to Pb, Sn and Ge are smaller in size. Therefore, when Sn and Ge are included, the bond lengths of Sn−I and Ge−I are smaller than those of Pb−I. We anticipate that this results in octahedral

Received: April 5, 2024
Revised: August 5, 2024
Accepted: August 8, 2024
Published: August 21, 2024

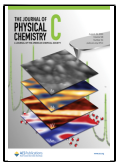

distortions, which leads to different interactions in local environments. It is well established that changes in perovskite octahedra geometry significantly impact the electronic structure.[23,24]

Moreover, the 3-AMPY cations interact with the anion slabs via the interaction between the terminal iodine atoms. The strength of this interactions (electrostatic) is sensitive to distances b/n the 3-AMPY and terminal iodine atoms.[18] Therefore, any changes in octahedral geometry would result in either increased or decreased electrostatic interactions between the organic cation part and inorganic part. Thus, doping $(3\text{-AMPY})_4$ Pb_4I_{16} with Sn/Ge in place of Pb likely changes the electronic structure and depicts the organic cation direct contributions to the electronic structure which is not observed much in conventional OIHP.

In this study, nine configurations of 2D slightly shifted DJ phase OIHP, namely, $(3\text{-AMPY})_4$ Pb_4I_{16}, $(3\text{-AMPY})_4$ $Pb_{4-x}Ge_xI_{16}$, and $(3\text{-AMPY})_4Ge_{4-x}Sn_xI_{16}$ (x = 1−4) were examined. We investigated their structural, electronic, optical, and photovoltaic properties using standard and time-dependent density functional theory. Our aim is to contribute in merging the stability advantages of synthesized $(3\text{-AMPY})_4PbI_{16}$ and environmental issues by modeling Pb-free configurations. We obtained enhanced PCE and maintained structural stability when Pb was replaced with the environmentally benign elements such as Ge and Sn atoms.

2. COMPUTATIONAL DETAILS

The first principle calculations of structural and electronic properties are performed using plane wave and projector augmented wave method in GPAW code.[25] A supercell consisting of 92 atoms of the structure of $(3\text{-AMPY})_4Pb_{4-x}I_{16}$ (x = Ge, Sn) was used under the periodic boundary conditions. Plane wave basis set cutoff energy is set to 600 eV, and a core electron is treated with PAW modality. We have used exchange and correlation (xc) functionals viz. generalized gradient approximation (GGA with PBE)[26] and DFT-D3[27] for structural and electronic property calculations. The effects of spin−orbit coupling (SOC) are also included in the electronic property calculations. Since the GGA-PBE functional approximation underestimates the electronic band gap, we also used GLLBSC including Kohn−Sham single-particle energy gap and derivative discontinuity[28] to determine the band gap. K-points of 4 × 4 × 1 Monkhorst−Pack grids[29] have been used for optimizing the structures and electronic property calculations.

The experimental cell parameters were kept constant for the $(3\text{-AMPY})_4PbI_{16}$ structure. In contrast, ions were allowed to relax using Broyden−Fletcher−Goldfarb−Shanno (BFGS)[30] algorithm until the forces between each atom were less than 0.03 eV/Å. Upon Sn/Ge doping, complete cell optimizations are performed with energy and force convergence of 0.001 meV and 0.03 eV/Å respectively.

Based on optical property calculations, we used a plane wave program package Quantum Espresso (QE)[31] to extract real and imaginary part of the dielectric function data. Norm conserving, pseudopotential were used to treat electron−ion interactions.[32] PBE exchange and correlation functionals along with a k-point sampling of 6 × 6 × 1 were used, resulting in convergence.

The formation energy is calculated as follows

$$E_{f(x,y)} = E(3\text{-AMPY})Pb_{4-x-y}Ge_xI_8 - (4-x-y)E(PbI_2) - xE(GeI_2) - 8E(HI) - 4E(3\text{-AMPY}) \quad (1)$$

where $0 \le x \le 4$ and $0 \le y \le 4$; a supercell of 10 formula units is used, and SnI_2, $(3AMPYGe_{4-x-y}Sn_xI_8)$ are used in place of GeI_2 and $(3\text{-AMPY})Pb_{4-x-y}Ge_xI_8)$, respectively, when Sn substitutes Ge.

The formation energy calculation method employed here has also been used in similar studies of OIHP.[23] Furthermore, ab initio molecular dynamics simulations (AIMD) were performed in the NVT ensemble at a temperature of 300 K with a Nose−Hoover thermostat. We have performed 10 ps simulations with a time step of 1 fs.

A frequency-dependent dielectric function is computed to shade light to the optical properties. The dielectric function is complex and can be expressed as

$$\boldsymbol{E}(\omega) = \varepsilon_1(\omega) + i\varepsilon_2(\omega) \quad (2)$$

The ε_2 is the imaginary part calculated using the density matrix of occupied and unoccupied wave functions over the Brillouin zone. ε_1 the real part was calculated using the Kramer−Kronig law from the imaginary part. The details of the formalism are given in.[33] Using the ε_1 and ε_2 data from QE calculations, we can determine the absorption characteristics using the expression

$$\alpha(\omega) = \sqrt{2}\frac{\omega}{c}[\sqrt{\varepsilon_1(\omega)^2 + \varepsilon_2(\omega)^2} - \varepsilon_1(\omega)]^{1/2} \quad (3)$$

The modeled configurations' photovoltaic performance is calculated using spectroscopic limited maximum efficiency (SLME) method proposed by Yu and Zunger.[34] SLME is analogous to the Shockley−Queisser limit (SQ),[35] conversely, the SLME considers the materials' absorbance property and thickness, in addition to the band gaps, only considered by SQ. The equations to calculate spectroscopic limited efficiency η are as follows

$$\eta = \frac{P_m}{P_{in}} \quad (4)$$

where P_m is the maximum power is output power density and P_{in} is the total incident solar power density. P_m is obtained by maximizing the total current density ($J = Jsc - J_0(e^{eV/k_BT} - 1)$ for a solar cell under a photon of flux I_{sun}) and voltage (V) characteristics as follows

$$P = JV = (J_{sc} - J_0(e^{eV/k_BT} - 1))V \quad (5)$$

where k_B and T represent the Boltzmann constant and temperature. J_{sc} is the short-circuit current density and is calculated as follows

$$J_{sc} = e\int_0^\infty (1 - e^{-2\alpha(E)L})I_{sun}dE \quad (6)$$

Here, $\alpha(E)$ and L stand for absorption coefficients at photon energy E and thickness of the absorbing layer, respectively. J_0 is the total reverse saturation current density and corresponds to the total electron−hole recombination current density at equilibrium. It is calculated as follows

$$J_0 = \frac{e}{f_r}\int_0^\infty (1 - e^{-2\alpha(E)L})I_{bb}(E, T)dE;\ \frac{1}{f_r} = e^{-\Delta E_g/k_BT} \quad (7)$$

https://doi.org/10.1021/acs.jpcc.4c02098
J. Phys. Chem. C 2024, 128, 14158−14167

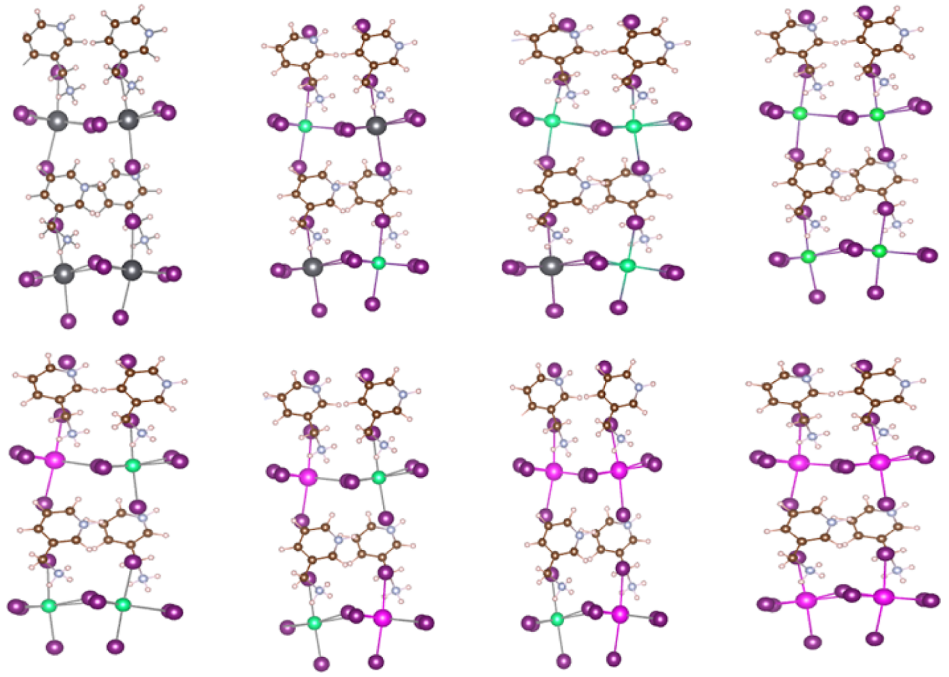

Figure 1. Relaxed structures of 2D perovskite systems investigated in this study. The top row illustrates the structures of $(3\text{-AMPY})_4Pb_{4-x}Ge_xI_{16}$ (x = 0, 2, 3, 4), while the bottom row is the structures of $(3\text{-AMPY})_4Ge_{4-x}Sn_xI_{16}$ (x = 1, 2, 3, 4). Atom colors: Pb = shiny gray (top row), Ge = light green (top and bottom rows), and Sn = rose (bottom panel).

Table 1. Calculated Crystal Structure Parameters, Volume, and Formation Energy Data

structure	a (Å)	b (Å)	c (Å)	β (deg)	V (Å^3)	FE (eV)	ref
Pb_4I_{16}	9.25	8.77	20.06	90.1	1629	−3.920	
Pb_4I_{16}	9.12[a]	8.78[a]	19.83[a]	90.1[a]	1588[a]	−3.64[b]	a = 16 b = 20
$GePb_3I_{16}$	9.12	8.77	19.83	90.1	1589	−3.72	
$Ge_2Pb_2I_{16}$	9.15	8.58	19.9	90.1	1564	−3.43	
$Ge_3Pb_1I_{16}$	9.11	8.68	19.81	90.1	1568	−3.11	
Ge_4I_{16}	9.09	8.38	19.75	90.1	1506	−2.77	
$Ge_2Sn_2I_{16}$	9.11	8.75	19.82	90.1	1581	−2.83	
$GeSn_3I_{16}$	9.11	8.77	19.83	90.1	1586	−3.01	
Sn_4I_{16}	9.12	8.77	19.83	90.1	1588	−3.15	

Here, I_{bb}, f_r^{-1}, and ΔE_g represent photon flux from blackbody radiation, the fraction of radiative recombination current, and ΔE_g the difference between direct and indirect allowed transition gap energy. The absorptivity data obtained using eq 3 are substituted for $\alpha(E)$. Standard AM1.5G (I_{sun}) solar irradiance at T = 25 °C data is used to obtain I_{bb}.

The open-circuit voltage, which is calculated under zero total current density condition data, is obtained as follows:

$$V_{oc} = \frac{k_B T}{e} \ln\left(1 + \frac{J_{sc}}{J_0}\right) \tag{8}$$

3. RESULTS AND DISCUSSION

3.1. Structural Properties and Stability Analysis. The PBE-optimized structures of the 2D perovskite systems studied in this work are shown in Figure 1. The structural data for the pristine $(3\text{-AMPY})_4Pb_4I_{16}$ are obtained from XRD measurement, and it crystallizes in the monoclinic crystal symmetry with space group of Pn.[18] The $(3\text{-AMPY})_4Pb_4I_{16}$ structure possesses a slightly offset DJ-phase arrangement, consisting of PbI_6 octahedra and disordered (3-AMPY) cations. This structure was used for the starting DFT input geometries. The doping of Pb in $(3\text{-AMPY})_4Pb_4I_{16}$ perovskite is achieved by substituting Ge/Sn atoms in place of Pb atoms.

The calculated lattice parameters, angles, volume, and formation energy data along with experimental data are given in Table 1. It appears that slight changes in the lattice constants are observed when Pb is doped with Ge and Sn.

Significant structural changes are observed in the octahedral geometry when Ge/Sn is doped in place of Pb in the pristine $(3\text{-AMPY})_4Pb_4I_{16}$. Structural changes in perovskite octahedra geometry can be characterized via M-I-M M (M = Pb, Ge, and Sn) bridging angle and terminal I···I contact distances between the layers. The calculated average Pb−I−Pb bridging angle and closest terminal I···I contact distances of $(3\text{-AMPY})_4Pb_4I_{16}$ are 160.1° and 4.26 Å (see Figure S1), respectively, which is in reasonable agreement with the experimental values of 170° and 4.16 Å[18] and in excellent agreement with other theoretical work 160° and 4.2 Å,[23] respectively. The doping of Ge and Sn resulted in a notable decrease in the bond lengths between Ge−I and Sn−I, in comparison to that of Pb−I. This decrease can be attributed to the variation in atomic sizes among Pb, Ge, and Sn. The smaller atomic sizes of Ge and Sn relative to Pb lead to a more compact arrangement, causing a reduction in the bond lengths between M-I. As a result, the octahedral

https://doi.org/10.1021/acs.jpcc.4c02098
J. Phys. Chem. C 2024, 128, 14158−14167

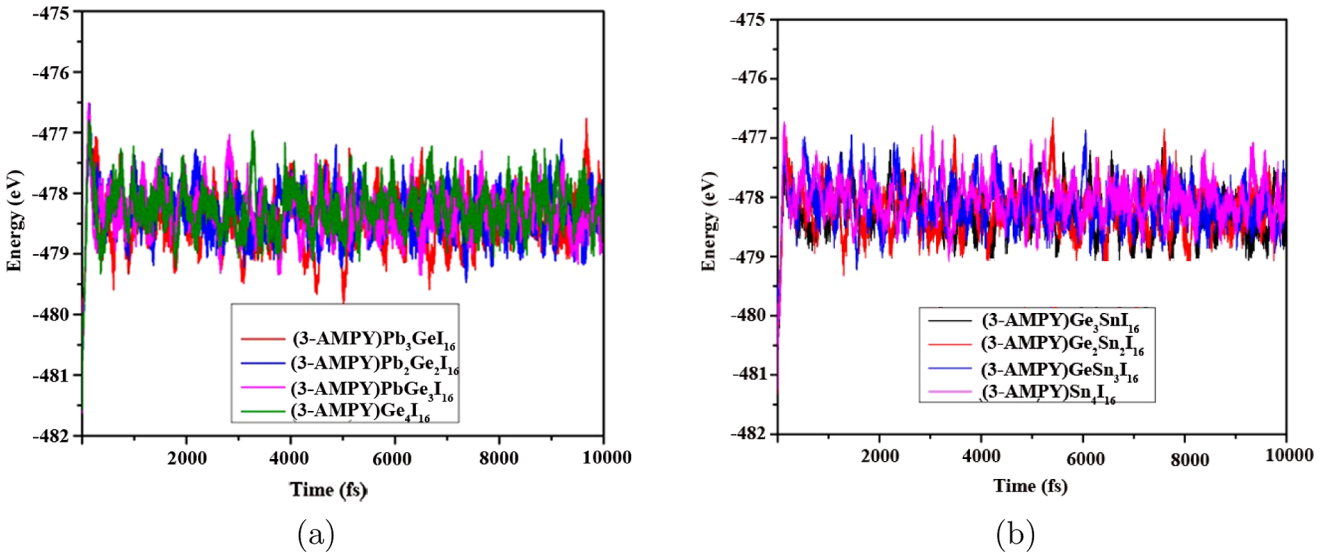

Figure 2. Variation of energy with simulation time for $(3\text{-AMPY})_4Pb_{4-x}Ge_xI_{16}$ (x = 1, 2, 3, 4) the first plot, and $(3\text{-AMPY})_4Ge_{4-x}Sn_xI_{16}$, the second plot left to right.

configuration undergoes a significant contraction, owing to the atomic size differences between the dopants (Ge and Sn) and Pb. Such changes in the octahedral structure lead to the modification of the M-I-M bridging angle, which further determines the symmetric nature of the structure. When Ge is doped into the pristine structure, the average bridging angle between M−I−M undergoes an increase from the pristine value of 160.1° to approximately 163.1°, the plots are presented in Figure S2. The angle further increases to a maximum value of 166.3° as the number of Ge increases. Sn−Ge configurations also show increased average bridging angle comparing to the pristine. However, the average bridging angle maintains a consistent value of 166° as the number of Sn increases. The closest terminal I···I contact distances between the layers were measured upon doping Ge (1−4) and Sn (1−4). The measured distances for these doping levels were determined to be 4.26, 4.26, 4.44, and 4.34 Å for Ge (1−4), respectively (Figure S2a). Subsequently, the replacement of Ge with Sn as a dopant led to an increase in the contact distance to 4.45 Å. However, upon fully doping Sn in place of Ge, the contact distance gradually decreased to 4.28 Å (Figure S2b).

The AIMD simulation results presented in Figure 2 indicate that these materials are stable at room temperature, demonstrating that Ge/Sn doping does not change the structure to new phase immediately.

3.2. Electronic Properties. The electronic band gap and band structure are crucial to determine the potential application of the model perovskites for photovoltaic. We have calculated the band gaps of 2D perovskite systems with GGA-PBE and GLLBSC + SOC levels, and the results are provided in Table 2. The calculated band gap for $(3\text{-AMPY})_4Pb_4I_{16}$ is 2.24 eV using the GLLBSC + SOC functional, which is in reasonable agreement with the experimental band gap of 2.34 eV[18] and in excellent agreement with the theoretical work of Mahal et al., who reported a band gap value of 2.28 eV from HSE + SOC calculations.[20]

As shown in Table 2, the band gap of doped Sn and Ge in $(3\text{-AMPY})_4Pb_4I_{16}$ decreases compared to that of the pristine value. This decrease follows a systematic trend; as the composition of Ge in $(3\text{-AMPY})_4Pb_4 - xGe_xI_{16}$ increases,

Table 2. Calculated Band Gap Value Data (in eV) of the 2D Perovskites

perovskite	GGA-PBE	GLLBSC + SOC	experimental
$(3\text{-AMPY})_4Pb_4I_{16}$	1.60	2.24	2.34[18]
$(3\text{-AMPY})_4Pb_3GeI_{16}$	1.57	1.94	
$(3\text{-AMPY})_4Pb_2Ge_2I_{16}$	1.55	1.95	
$(3\text{-AMPY})_4PbGe_3I_{16}$	1.50	1.86	
$(3\text{-AMPY})_4Ge_4I_{16}$	1.48	1.87	
$(3\text{-AMPY})_4Ge_3SnI_{16}$	1.28	1.69	
$(3\text{-AMPY})_4Ge_2Sn_2I_{16}$	1.35	1.64	
$(3\text{-AMPY})_4GeSn_3I_{16}$	1.17	1.35	
$(3\text{-AMPY})_4Sn_4I_{16}$	0.95	1.30	

the band gap decreases from its initial value of 2.24 eV for pristine $(3\text{-AMPY})_4Pb_4I_{16}$ to 1.86 eV for $(3\text{-AMPY})_4Ge_4I_{16}$. The band gap value decreases further with Sn substitution, reaching 1.30 eV for the fully Sn-substituted structure, $(3\text{-AMPY})_4Sn_4I_{16}$. The decrease in band gap with Sn substitution renders these materials for photovoltaic applications.

In order to understand the effects of Ge and Sn doping on band gap changes, total and partial density of states (PDOS) data are plotted and presented in Figure 3a,b respectively. The results indicate two fundamental characteristics of halide perovskite strong optical transitions: (i) p−p/s-p transitions and (ii) direct band gap.[36] In addition, the organic cation's direct contribution to the electronic structure is observed.

The PDOS of $(3\text{-AMPY})_4Pb_4I_{16}$ shows that the I-5p orbital has the maximum contribution to the valence band maximum (VBM) and C-2p has the maximum contribution to the conduction band minimum (CBM). After increasing the Ge-concentration, the VBM and CBM edges shift toward the Fermi level. The orbital contributions from Pb-6s and Ge-4s in VBM are observed while the unoccupied C-2p orbital contributes to the conduction band edges near the Fermi level. In $(3\text{-AMPY})_4Pb_4I_{16}$, the C-2p orbitals were found at 0.39 eV (see Figure S3) above the Fermi level in CB. Upon Ge concentration increases, the C-2p orbital intensity increases and shifts to the Fermi level (see Figure 3a).

The full substitution of Pb in the $(3\text{-AMPY})_4Pb_4I_{16}$ lattice by Ge results in the significant shift of the C-2p orbitals to the

https://doi.org/10.1021/acs.jpcc.4c02098
J. Phys. Chem. C 2024, 128, 14158−14167

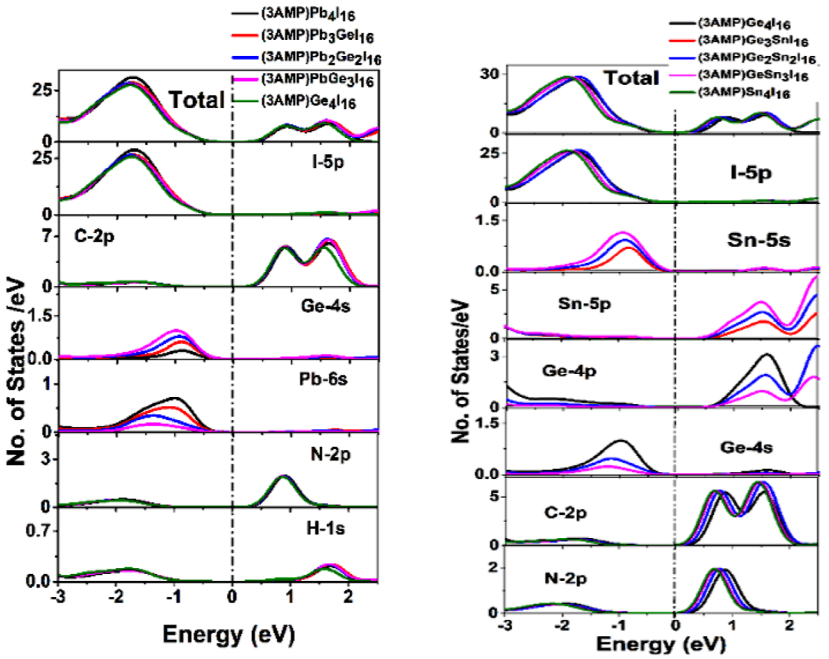

Figure 3. Total and PDOS for $(3\text{-AMPY})_4Ge_{4-x}Sn_xI_{16}$ (a) and $(3\text{-AMPY})_4Ge_{4-x}Sn_xI_{16}$ (x = 1, 2, 3, 4) (b).

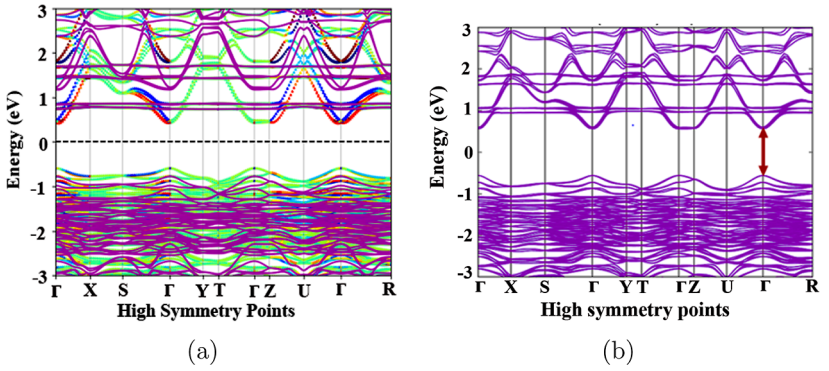

Figure 4. Band structure data, using the PBE + SOC. The first plot is $(3\text{-AMPY})_4Pb_4I_{16}$, this study and the second plot is $(3\text{-AMPY})_4Pb_4I_{16}$, adapted with permission from the work of Mahal E. et al., using PBE + SOC.[23] The Fermi energy level is adjusted to zero. The coordinates of high symmetry points of Brillouin zones for all modeled structures in this study are given in Figure S5.

Fermi level and is located at 0.206 eV (see Figure S3) above the Fermi level. The electrons from ns^2 are lone pair electrons and hence result in p−p transitions. Furthermore, 4s electrons from Ge act as a doping level and result in the transition of electrons from I-5p and Pb-6s orbitals to the C-2p orbital. These strong p−p and s-p transitions result in reductions of the band gap by pulling the CBM edges toward the Fermi level.

For Ge substitution by Sn in the $(3\text{-AMPY})_4Ge_4I_{16}$ lattice, similar behavior is observed with Pb substitution by Ge in $(3\text{-AMPY})_4Pb_4I_{16}$, and the band gap for Sn-containing systems is much smaller than those for the Pb−Ge and fully Ge-containing configurations. The plots are presented in Figure 3b.

The I-5p orbitals and small contributions from Sn and Ge 5s orbitals dominate the VBM. With increased Sn concentrations, the unoccupied N-2p orbital edge significantly shifts toward the Fermi level, unlike the Pb−Ge containing conformer, where significant shifts of C-2p orbitals to the Fermi level were observed (see Figure S4c). This indicates direct p−p electronic transitions. Moreover, the presence of Ge and Sn lone pair electrons in the VBM facilitates strong p−p transitions in Ge−Sn containing configurations, resulting in a smaller band gap.[36] The implication of this is that very strong optical absorption in Ge−Sn and strong optical absorption in Pb−Ge containing structures is expected.

The obtained band structure data for all of the evaluated systems are presented. Two major properties that are suitable for photovoltaic applications are observed from the characteristics of energy levels at high symmetry points of Brillouin zones: (i) direct band gaps at gamma points and (ii) dispersive VBM edges. For the pristine (see Figure 4) and Ge−Pb (see Figure 5a−c) configurations, the conduction and valence band edges show a highly dispersive nature which indicates the high mobility of the photogenerated carriers in the crystal. As the Ge content increases, the conduction band minima edges shift, leaving the electronic states for organic cations (Figure 5a−d). This is because decreased Pb content in $(3\text{-AMPY})_4Pb_4I_{16}$ results in conduction band minima mainly constituting the organic cation spacer due to a decreased SOC effect associated

https://doi.org/10.1021/acs.jpcc.4c02098
J. Phys. Chem. C 2024, 128, 14158−14167

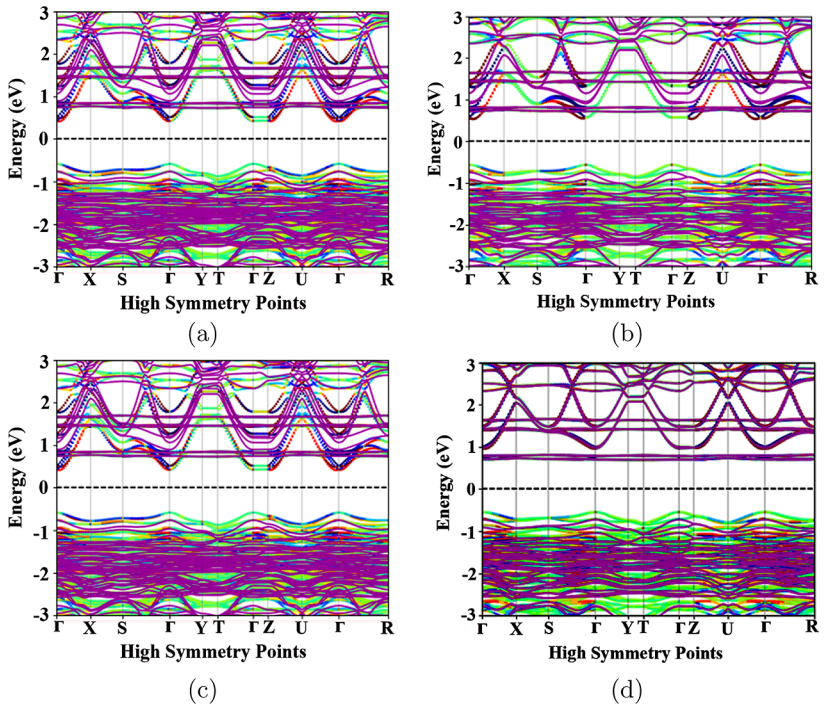

Figure 5. Band structure data for $(3\text{-AMPY})_4Pb_{4-x}Ge_xI_{16}$ (x = 1, 2, 3, 4) using PBE + SOC. The top row displays the band structure for x = 1 and x = 2 from left to right, respectively. The bottom row displays the band structure for x = 3 and x = 4 left to right, respectively. The Fermi energy level is adjusted to zero.

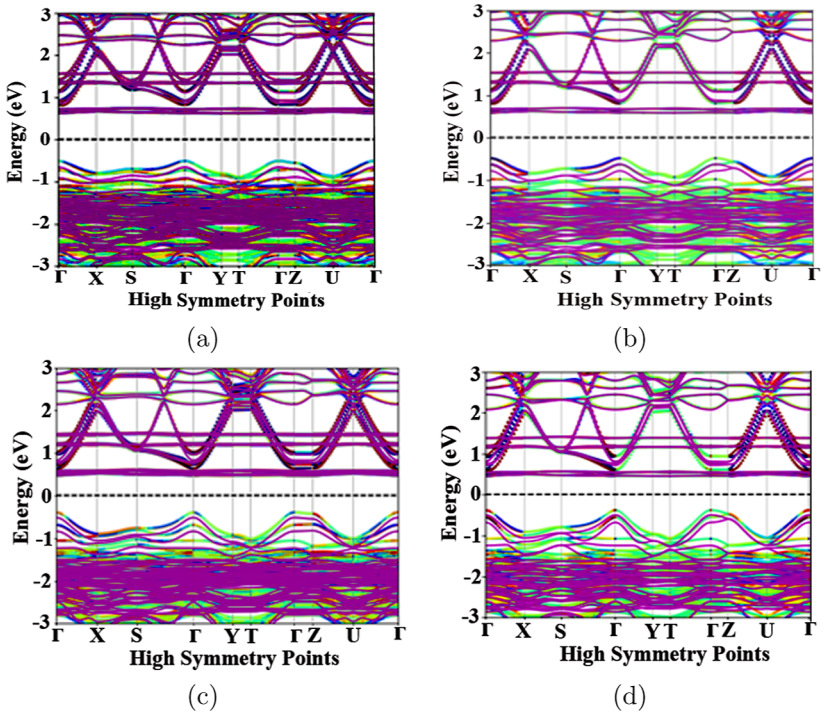

Figure 6. Band structure data for $(3\text{-AMPY})_4Ge_{4-x}Sn_xI_{16}$ (x = 1, 2, 3, 4) using PBE + SOC. The top row displays the band structure for x = 1 and x = 2 from left to right, respectively. The bottom row displays the band structure for x = 3 and x = 4 left to right, respectively. The Fermi energy level is adjusted to zero.

with Pb. The organic cation exhibits a flat stabilized band structure, attributed to its low dielectric nature compared to the inorganic moiety. Additionally, the presence of strong p−p transitions coupled with closer proximity of Ge and I orbit bond lengths when compared with Pb−I bond results in strong s−p coupling, which becomes stronger at the gamma point and results in the direct band gap.

The band structure data for Ge−Sn containing configurations are presented in Figure 6. The CBM mainly consists of organic cation spacers and is less dispersive, while a highly dispersive VBM was observed. Upon increasing Sn concen-

https://doi.org/10.1021/acs.jpcc.4c02098
J. Phys. Chem. C 2024, 128, 14158−14167

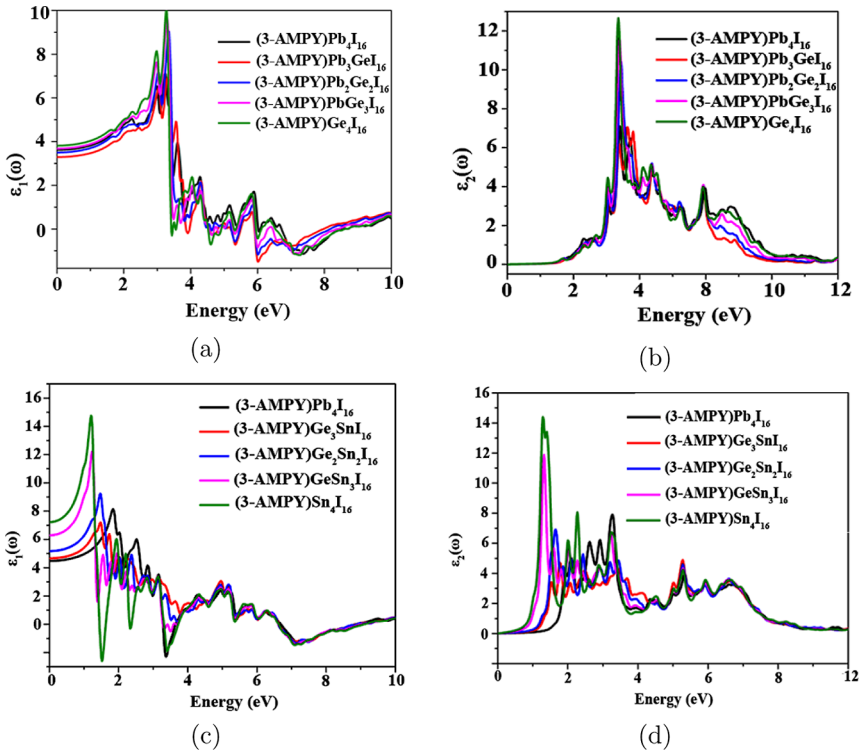

Figure 7. Dielectric function analysis of $(3\text{-AMPY})_4Pb_{4-x}Ge_xI_{16}$ (x = 1, 2, 3, 4) and $(3\text{-AMPY})_4Ge_{4-x}Sn_xI_{16}$ (x = 1, 2, 3, 4) as a function of photon energy in eV. (a) Real part (ε_1) and (b) imaginary part (ε_2) are presented for $(3\text{-AMPY})_4Pb_{4-x}Ge_xI_{16}$ (x = 1, 2, 3, 4). (c,d) Corresponding data for $(3\text{-AMPY})_4Ge_{4-x}Sn_xI_{16}$ perovskite.

trations, a significant shift of the VBM toward the Fermi level was observed. The bond length of Sn−I is shorter than Ge−I, resulting in closer proximity of I-5p and Sn-4s orbitals, which results in stronger s-p orbital coupling and a direct band gap at the Gamma point.

3.3. Optical Properties. In Figure 7, the real and imaginary dielectric constant data are presented. The results indicate improved two key features for applicability in the photovoltaic effect upon Ge/Sn doping: (i) high charge screening and (ii) visible light absorption range. The real part of the dielectric constant (ε_1) value at a static frequency (ω = 0) provides essential insights into the binding energy of exciton (electron−hole pairs); the higher the value is, associated with lower the occurrence of radiative recombination, which is highly beneficial for photovoltaic applications. The calculated real part of the dielectric constant at static frequency for $(3\text{-AMPY})_4Pb_4I_{16}$ is 3.6 eV. The dielectric constant falls below 3.6 eV, to values of 3.26 and 3.5 eV upon one and two Ge doping, respectively. However, upon three and four Ge doping, the value increases to 3.67 and 3.8 eV, respectively. This implies that the full doping of Pb in $(3\text{-AMPY})_4Pb_4I_{16}$ by Ge increases the static dielectric constant (at ω = 0) for the real part. The implication is that the fully Ge-containing conformer exhibits improved electron−hole radiative recombination which results in high charge screening. The imaginary part (ε_2) of the dielectric function is also shown in Figure 7b, which shows the radiation absorbed by the material. Figure shows that the curve rises after the energy values pass through the band gap energy values. The main peaks are observed between energy values of 2−4 eV, which encompass the majority of the visible light spectrum region, making it a suitable candidate for photovoltaic application.

Figure 7c,d presents the dielectric function for the Sn-substituted configurations. Compared with the pristine-Ge, and fully Ge-doped systems, an enhanced optical property for photovoltaic applications from the (ε_1) part of the dielectric functions is observed. A significant increase in the (ε_1) peak intensity is depicted in the visible light region upon increasing Sn content coupled with increasing static dielectric constant. The obtained values of (ε_1) (at ω = 0) are 6.32, 5.21, 4.73, and 7.3 eV which are higher than those of pristine, Pb−Ge, and fully Ge containing conformers upon increasing Sn concentration from (1−4), respectively. From imaginary part of the dielectric function, it looks that pronounced absorption characteristics are shifted to infrared region upon increasing Sn concentration. This is due to the gradual decrease in band gap with increasing Sn concentrations. This behavior is observed in related research studies.[19,37] Using the real and imaginary parts of the dielectric function, the absorption properties are evaluated by using eq 3, and the plots are presented in Figure 8. The fully Ge-containing conformer exhibits a blue-shifted maximum absorption characteristic, while the fully Sn-containing conformer shows an enhanced absorption peak in the visible light region. It should be noted that the absorption spectrum alone cannot be used to determine the structure with the maximum PCE for solar cell applications as such, we calculated the SLME.

3.4. Spectroscopic Limited Maximum Efficiency. We calculated the PCE for all modeled configurations using eqs 4, 5, 6, and 7 and open-circuit voltage using eq 8. The calculated results are presented in Figures 8 and S6, respectively. The open-circuit voltage (V_{oc}) for Pb−Ge containing configurations decreases monotonically with increasing absorbing layer thickness. $(3\text{-AMPY})_4Pb_4I_{16}$ exhibits the maximum open-circuit voltage value of 1.9 V. This can be attributed to the

https://doi.org/10.1021/acs.jpcc.4c02098
J. Phys. Chem. C 2024, 128, 14158−14167

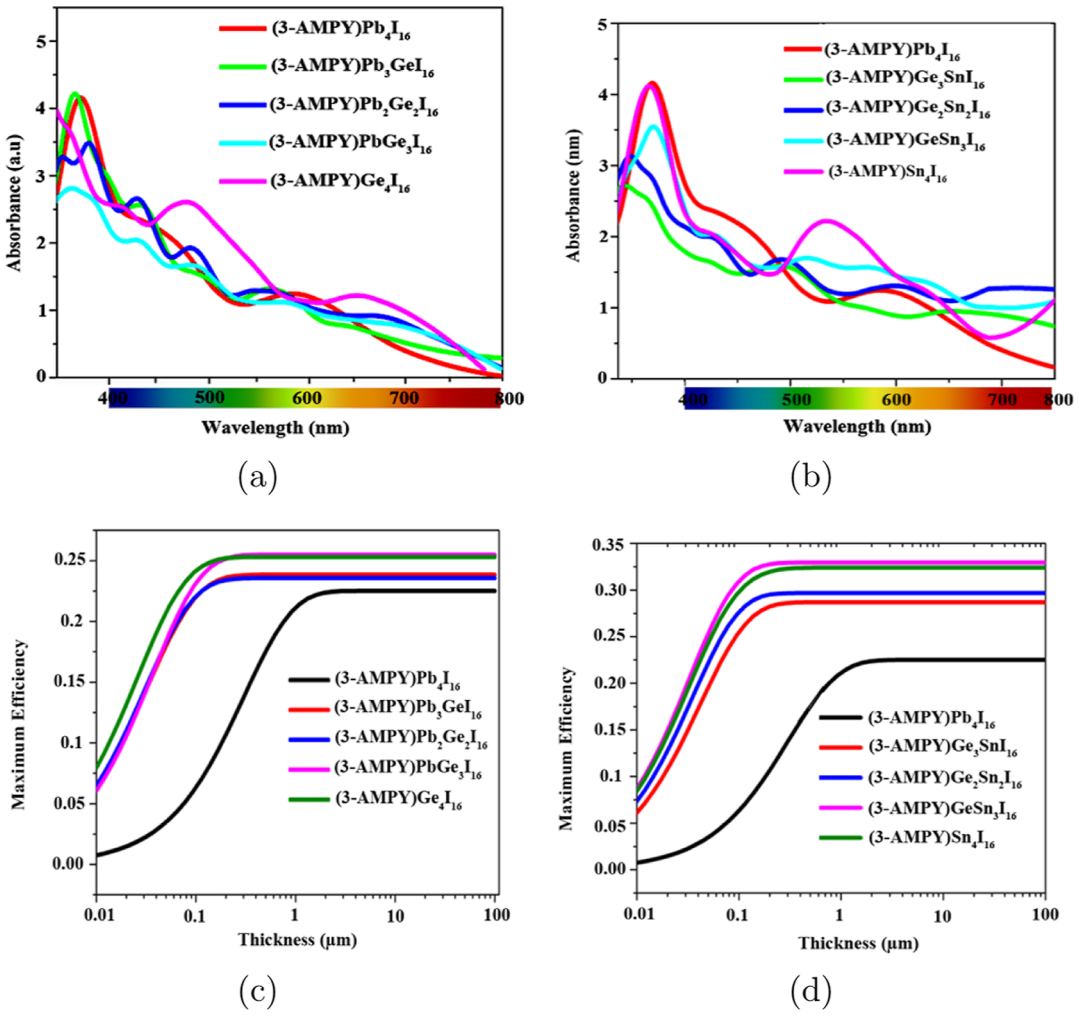

Figure 8. Visible absorption coefficient (a) for $(3\text{-AMPY})_4Pb_{4-x}Ge_xI_{16}$ (x = 1, 2, 3, 4) and (b) for $(3\text{-AMPY})_4Ge_{4-x}Sn_xI_{16}$ (x = 1, 2, 3, 4) perovskite. (c,d) Corresponding data for PCE versus absorber layer.

large band gap as Ge/Sn doping reduces the band gap. The respective values of V_{oc} for $(3\text{-AMPY})_4Pb_4{-}xGe_xI_{16}$ (x = 1, 2, 3, 4) are 1.62, 1.63, 1.55, and 1.55 V (see Figure S6a). The corresponding data of V_{oc} for Ge−Sn containing configurations are also given in Figure S6b. The Ge−Sn containing configurations exhibit lower open-circuit voltage compared to the pristine and Pb−Ge containing configurations. For$(3\text{-AMPY})_4Ge_{4-x}Sn_xI_{16}$ (x = 1, 2, 3, 4) with x = 1, 2, 3, and 4, the respective open-circuit voltage values are 1.39, 1.34, 1.07, and 1.022 V. Unlike the other configurations, the V_{oc} values for $(3\text{-AMPY})_4GeSn_3I_{16}$ and $(3\text{-AMPY})Sn_4I_{16}$ show increasing trend as the absorbing layer thickness increases. Understanding the V_{oc} variations provides crucial insights into their photovoltaic performance and overall efficiency. However, the V_{oc} is not the only parameter that determines the power of producing high efficiency. It showed that the Ge and Sn doping substantially improves the efficiency of the 2D $(3\text{-AMPY})_4Pb_4I_{16}$-based perovskites. As the concentration of Ge increases, the efficiency increases from 22.5−25.5%. A high efficiency of 25.5% is recorded upon fully Ge doping in $(3\text{-AMPY})_4Pb_4I_{16}$. Additionally, $(3\text{-AMPY})_4Pb_3Ge$, $(3\text{-AMPY})_4Pb_2Ge_2$, and $(3\text{-AMPY})_4PbGe_3$ show remarkable efficiencies of 23.9, 23.6, and 25.5%, respectively. The efficiency trend aligns with the changes in the electronic band gap with the fully Ge-containing conformer exhibiting a band gap value ideal for visible light absorption.

The efficiencies of Sn-containing systems are very important as Pb substitution by Sn shows thermodynamic stability over Ge-containing systems, as shown in Table 1. Interestingly, the PCE shows the greatest improvement for Sn- and Ge-containing systems. It looks like Sn doping results in maximum improvement in PCE. From Figure 8d, one finds that $(3\text{-AMPY})_4GeSn_3I_{16}$ conformer exhibits maximum efficiency of 32.9% while the completely Sn containing conformer $(3\text{-AMPY})_4Sn_4I_{16}$ exhibits PCE of 32.4%. The difference is attributed to the smaller band gap value of $(3\text{-AMPY})_4Sn_4I_{16}$ which falls below the ideal band gap value of single junction solar cell (1.1 eV).[35] Also, $(3\text{-AMPY})_4SnGe_3$ and $(3\text{-AMPY})_4Sn_2Ge_2$ exhibit remarkable PCE values of 28.6 and 29.6%, respectively. In general, Sn/Ge doping leads to improved PCE, with Sn doping values that surpass those reported in other perovskite materials.[19,37,38]

4. CONCLUSIONS

In summary, we have calculated the structural, electronic, optical, and photovoltaic performance properties of 2D slightly shifted DJ phase $(3\text{-AMPY})_4Pb_4I_{16}$ perovskites for solar cell applications. The band gap was calculated using the PBE, PBE + SOC, and GLLBSC + SOC functional. The accurate

https://doi.org/10.1021/acs.jpcc.4c02098
J. Phys. Chem. C 2024, 128, 14158−14167

determination of the band gap is very important as the optical property calculation resides on the values of the band gap. Due to the inherent complexity of the OIHP structure and the substantial number of atoms involved (92 atoms) in our system, we were unable to conduct more precise calculations using hybrid functional or GW methods to determine the band gap. Similarly, advanced optical property calculations utilizing the Bethe−Salpeter equation (BSE) method were also computationally expensive. However, we systematically calculated the optical properties using the GGA-PBE functional. The SOC effect is known to reduce the band gap, but for our system, the SOC effect is a function of the Pb atom. Since we are replacing the Pb atom with lighter elements, the SOC effect on the band gap is negligible for our optical property calculation. Therefore, if one were to use heavy methods such as GW or BSE, the calculated properties would be similar to our results.

The main purpose of this study is to evaluate the electronic and optical properties of slightly shifted DJ phase (3-AMPY)$_4$Pb$_4$I$_{16}$ perovskites upon substitution of Pb by Sn and Ge to address Pb toxicity. Additionally, we evaluated whether the introduction of Sn and Ge atoms resulted in improved performance for solar applications. The substitution of Pb by Sn and Ge shows changes in the electronic properties as well as optical properties. The band gap decreased with Sn and Ge substituting Pb in the (3-AMPY)Pb$_4$I$_{16}$ lattice, and the maximum PCE was found for the Pb-free configuration. The Pb-free (3-AMPY)$_4$GeSn$_3$I$_{16}$, (3-AMPY)Sn$_4$I$_{16}$, and (3-AMPY)Sn$_2$Ge$_2$I$_{16}$ configurations show high PCEs of 32.9, 32.4, and 29.6%, respectively. Thus, the toxicity issues of the stable slightly shifted DJ phase (3-AMPY)$_4$PbI$_{16}$ can be addressed via Ge and Sn substitution.

■ ASSOCIATED CONTENT

Supporting Information

The Supporting Information is available free of charge at https://pubs.acs.org/doi/10.1021/acs.jpcc.4c02098.

Structural data (3-AMPY)$_4$Pb$_4$I$_{16}$ with bridging angle, bond length between Pb−I, closest I···I terminal distance, and closest NH_3^+···I distances, and rose-colored plane indicating the penetration depth of terminal NH_3^+; structural data for (3-AMPY)$_4$Pb$_{4-x}$Ge$_x$I$_{16}$ (x = 1, 2, 3, 4) with bridging angle, bond length between M−I (M = Pb, Ge, and Sn) closest I···I terminal distance, and closest NH_3^+···I distances; rose-colored plane indicating the penetration depth of terminal NH_3^+; corresponding data for (3-AMPY)$_4$Ge$_{4-x}$Sn$_x$I$_{16}$ (x = 1, 2, 3, 4); and rose-colored atom tin (Sn); total density of states, I-5p, N-2p, and C−2p partial density of states for (3-AMPY)$_4$*Pb*$_{4-x}$Ge$_x$I$_{16}$ (x = 1, 2, 3, 4); total density of states, I−5p, N−2p, and C−2p partial density of states for (3-AMPY)$_4$Ge$_{4x}$Sn$_x$I$_{16}$ (x = 1, 2, 3, 4); path of high symmetry points of the Brillouin zone; open-circuit voltage for (3-AMPY)$_4$Pb$_{4-x}$Ge$_x$I$_{16}$ (x = 0, 1, 2, 3, 4) and corresponding data for (3-AMPY)$_4$Ge$_{4-x}$Sn$_x$I$_{16}$ (x = 1, 2, 3, 4) PDF)

■ AUTHOR INFORMATION

Corresponding Authors

Yedilfana Setarge Mekonnen − *Center for Environmental Science, College of Natural and Computational Sciences, Addis Ababa University, Addis Ababa 1000, Ethiopia;* orcid.org/0000-0001-9331-7370; Email: yedilfana.setarge@aau.edu.et

Kingsley Onyebuchi Obodo − *Center for Space Research, North-West University, Potchefstroom 2531, South Africa; ICTP-East African Institute for Fundamental Research, Kigali City 00000, Rwanda; National Institute of Theoretical and Computational Sciences, Johannesburg 2000, South Africa;* orcid.org/0000-0002-1428-2761; Email: obodokingsley@gmail.com

Authors

Frew Gashaw Asefa − *Materials Science Program, College of Natural and Computational Sciences, Addis Ababa University, Addis Ababa 1000, Ethiopia*

Aseres Alula Arega − *Materials Science Program, College of Natural and Computational Sciences, Addis Ababa University, Addis Ababa 1000, Ethiopia*

Getachew Gizaw Kebede − *Materials Science Program, College of Natural and Computational Sciences, Addis Ababa University, Addis Ababa 1000, Ethiopia*

Complete contact information is available at: https://pubs.acs.org/10.1021/acs.jpcc.4c02098

Notes

The authors declare no competing financial interest.

Published as part of The Journal of Physical Chemistry C special issue "Computational Sciences from Africa and the African Diaspora".

■ ACKNOWLEDGMENTS

This work was supported by a thematic research project (grant number TR/036/2021) sponsored by Addis Ababa University and the World Academy of Sciences (TWAS) (grant no. 19-202 RG/CHE/AF/AC_G). The authors would like to thank the Center for Functional Nanomaterials (CFN), which is a U.S. Department of Energy Office of Science User Facility, at Brookhaven National Laboratory under Contract no. DE-SC0012704 and project number 308379. The authors also thank the Ethiopian Education and Research Network (EthERNet) at the Ethiopian Ministry of Education. Moreover, Y.S.M. would like to acknowledge support from the ICTP through the Associates Programme (2020-2025).

■ REFERENCES

(1) Chen, C.; Zhao, X.; Gong, Y.; Liu, Y.; Chen, Z.; Zhang, L.; Chen, J.; Deng, Z.; Lu, H.; Luo, M.; et al. Two-Dimensional Hybrid Dion−Jacobson Germanium Halide Perovskites. *Chem. Mater.* **2023**, *35*, 3265−3275.

(2) Park, N. Research direction toward scalable, stable, and high efficiency perovskite solar cells. *Adv. Energy Mater.* **2020**, *10*, 1903106.

(3) Weber, D. $CH_3NH_3PbX_3$, ein Pb (II)-system mit kubischer perowskitstruktur/$CH_3NH_3PbX_3$, a Pb (II)-system with cubic perovskite structure. *Z. Naturforsch., B: J. Chem. Sci.* **1978**, *33*, 1443−1445.

(4) Jena, A. K.; Kulkarni, A.; Miyasaka, T. Halide perovskite photovoltaics: background, status, and future prospects. *Chem. Rev.* **2019**, *119*, 3036−3103.

(5) Ju, D.; Dang, Y.; Zhu, Z.; Liu, H.; Chue, C.; Li, X.; Wang, L.; Hu, X.; Jen, A. K.; Tao, X. Tunable Band Gap and Long Carrier Recombination Lifetime of Stable Mixed $CH_3NH_3Pb_xSn_{1-x}Br_3$ Single Crystals. *Chem. Mater.* **2018**, *30*, 1556−1565.

(6) Kober-Czerny, M.; Motti, S. G.; Holzhey, P.; Wenger, B.; Lim, J.; Herz, L. M.; Snaith, H. J. Excellent Long-Range Charge-Carrier Mobility in 2D Perovskites. *Adv.Funct. Mater.* **2022**, *32*, 2203064.

(7) Yang, T.; Gao, L.; Lu, J.; Ma, C.; Du, Y.; Wang, P.; Ding, Z.; Wang, S.; Xu, P.; Liu, D.; et al. One-stone-for-two-birds strategy to attain beyond 25% perovskite solar cells. *Nat. Commun.* **2023**, *14*, 839.
(8) Chen, C.; Ran, C.; Yao, Q.; Wang, J.; Guo, C.; Gu, L.; Han, H.; Wang, X.; Chao, L.; Xia, Y.; et al. Screen-Printing Technology for Scale Manufacturing of Perovskite Solar Cells. *Adv. Sci.* **2023**, *10*, 2303992.
(9) Kaltenbrunner, M.; Adam, G.; Głowacki, E. D.; Drack, M.; Schwödiauer, R.; Leonat, L.; Apaydin, D. H.; Groiss, H.; Scharber, M. C.; White, M. S.; et al. Flexible high power-per-weight perovskite solar cells with chromium oxide−metal contacts for improved stability in air. *Nat. Mater.* **2015**, *14*, 1032−1039.
(10) Song, Z.; McElvany, C. L.; Phillips, A. B.; Celik, I.; Krantz, P. W.; Watthage, S. C.; Liyanage, G. K.; Apul, D.; Heben, M. J. A technoeconomic analysis of perovskite solar module manufacturing with low-cost materials and techniques. *Energy Environ. Sci.* **2017**, *10*, 1297−1305.
(11) Chowdhury, T. A.; Bin Zafar, M. A.; Sajjad-Ul Islam, M.; Shahinuzzaman, M.; Islam, M. A.; Khandaker, M. U. Stability of perovskite solar cells: issues and prospects. *RSC.Adv.* **2023**, *13*, 1787−1810.
(12) Dipta, S. S.; Uddin, A. Stability issues of perovskite solar cells: A critical review. *Energy Technol.* **2021**, *9*, 2100560.
(13) Kar, M.; Sarkar, R.; Pal, S.; Sarkar, P. Lead free two-dimensional mixed tin and germanium halide perovskites for photovoltaic applications. *J.Phys.Chem. C* **2021**, *125*, 74−81.
(14) Zhang, X.; Wang, P.; Wu, Q.; Xu, L.; Chen, M.; Kang, Y.; Sun, C.; Wei, G.; Qiao, Z.; Lin, Z. Dion-Jacobson phase lead-free halide (PDA)MX4 (M=Sn/Ge; X=I/Br/Cl) perovskites: A first-principles theory. *J. Solid State Chem.* **2022**, *315*, 123449.
(15) Ahmad, S.; Fu, P.; Yu, S.; Yang, Q.; Liu, X.; Wang, X.; Wang, X.; Guo, X.; Li, C. Dion-Jacobson phase 2D layered perovskites for solar cells with ultrahigh stability. *Joule* **2019**, *3*, 794−806.
(16) Guo, W.; Yang, Z.; Dang, J.; Wang, M. Progress and perspective in Dion-Jacobson phase 2D layered perovskite optoelectronic applications. *Nano Energy* **2021**, *86*, 106129.
(17) Yang, L.; Chen, Y.; Wang, X.; Deng, J.; Wang, W.; Ding, X.; Yang, W.; Yao, J. First-Principles Study on the Stability and Electronic Properties of Dion−Jacobson Halide $A(MA)_{n-1}B_nX_{3n+1}$ Perovskites. *J.Phys.Chem. C:* **2021**, *125*, 24096−24104.
(18) Li, X.; Ke, W.; Traoré, B.; Guo, P.; Hadar, I.; Kepenekian, M.; Even, J.; Katan, C.; Stoumpos, C.; Schaller, R. D.; Kanatzidis, M. G.; et al. Two-dimensional Dion−Jacobson hybrid lead iodide perovskites with aromatic diammonium cations. *J. Am. Chem. Soc.* **2019**, *141*, 12880−12890.
(19) Kagdada, H. L.; Materny, A.; Singh, D. K. Decreasing toxicity and increasing photoconversion efficiency by Sn-substitution of Pb in 5-ammonium valeric acid-based two-dimensional hybrid perovskite materials. *Phys. Chem. Chem. Phys.* **2022**, *24*, 23226−23235.
(20) Ke, W.; Chen, C.; Spanopoulos, I.; Mao, L.; Hadar, I.; Li, X.; Hoffman, J. M.; Song, Z.; Yan, Y.; Kanatzidis, M. G. Narrow-bandgap mixed lead/tin-based 2D Dion−Jacobson perovskites boost the performance of solar cells. *J. Am. Chem. Soc.* **2020**, *142*, 15049−15057.
(21) Fu, H. Dion−Jacobson halide perovskites for photovoltaic and photodetection applications. *J. Mater. Chem. C: Mater.* **2021**, *9*, 6378−6394.
(22) Guan, M.; Xie, Y.; Zhang, Y.; Gu, Z.; Qiu, L.; He, Z.; Ye, B.; Suwardi, A.; Dai, Z.; Li, G.; et al. Moisture-Tailored 2D Dion−Jacobson Perovskites for Reconfigurable Optoelectronics. *Adv. mater.* **2023**, *35*, 2210611.
(23) Mahal, E.; Mandal, S. C.; Pathak, B. Band edge engineering of 2D perovskite structures through spacer cation engineering for solar cell applications. *J.Phys.Chem. C* **2022**, *126*, 9937−9947.
(24) Vardeny, Z. V.; Beard, M. C. *Hybrid Organic Inorganic Perovskites: Physical Properties and Applications*; World Scientific, 2022, *18*.
(25) Enkovaara, J.; Rostgaard, C.; Mortensen, J. J.; Chen, J.; Dułak, M.; Ferrighi, L.; Gavnholt, J.; Glinsvad, C.; Haikola, V.; Hansen, H. A.; et al. Electronic structure calculations with GPAW: A real-space implementation of the projector augmented-wave method. *J. Phys.: Condens. Matter* **2010**, *22*, 253202.
(26) Perdew, J. P.; Burke, K.; Ernzerhof, M. Generalized gradient approximation made simple. *Phys. Rev. Lett.* **1996**, *77*, 3865−3868.
(27) Grimme, S.; Antony, J.; Ehrlich, S.; Krieg, H. A consistent and accurate ab initio parametrization of density functional dispersion correction (DFT-D) for the 94 elements H-Pu. *J. Chem. Phys.* **2010**, *132*, 154104.
(28) Kuisma, M.; Ojanen, J.; Enkovaara, J.; Rantala, T. T. Kohn-Sham potential with discontinuity for band gap materials. *Phys. Rev. B* **2010**, *82*, 115106.
(29) Monkhorst, H. J.; Pack, J. D. Special points for Brillouin-zone integrations. *Phys. Rev. B* **1976**, *13*, 5188−5192.
(30) Head, J. D.; Zerner, M. C. A Broyden—Fletcher—Goldfarb—Shanno optimization procedure for molecular geometries. *Chem.-Phys.Lett.* **1985**, *122*, 264−270.
(31) Giannozzi, P.; Baroni, S.; Bonini, N.; Calandra, M.; Car, R.; Cavazzoni, C.; Ceresoli, D.; Chiarotti, G. L.; Cococcioni, M.; Dabo, I.; et al. QUANTUM ESPRESSO: a modular and open-source software project for quantum simulations of materials. *J. Phys.: Condens. Matter* **2009**, *21*, 395502.
(32) Hamann, D. R.; Schlüter, M.; Chiang, C. Norm-conserving pseudopotentials. *Phys. Rev. Lett.* **1979**, *43*, 1494−1497.
(33) Abeles, F. *Optical Properties of Metals*; North-Holland: Amsterdam, 1972.
(34) Yu, L.; Zunger, A. Identification of potential photovoltaic absorbers based on first-principles spectroscopic screening of materials. *Phys. Rev. Lett.* **2012**, *108*, 068701.
(35) Shockley, W.; Queisser, H. *Renewable Energy*; Routledge, 2018.
(36) Goyal, A.; McKechnie, S.; Pashov, D.; Tumas, W.; van Schilfgaarde, M.; Stevanović, V. Origin of pronounced nonlinear band gap behavior in lead−tin hybrid perovskite alloys. *Chem. Mater.* **2018**, *30*, 3920−3928.
(37) Wei, N.; Chen, Y.; Miao, Y.; Zhang, T.; Wang, X.; Wei, H.; Zhao, Y. 5-Ammonium Valeric Acid Iodide to Stabilize $MAPbI_3$ via a Mixed-Cation Perovskite with Reduced Dimension. *J. Phys. Chem. Lett.* **2020**, *11*, 8170−8176.
(38) Stoumpos, C. C.; Cao, D. H.; Clark, D. J.; Young, J.; Rondinelli, J. M.; Jang, J. I.; Hupp, J. T.; Kanatzidis, M. G. Ruddlesden−Popper hybrid lead iodide perovskite 2D homologous semiconductors. *Chem. Mater.* **2016**, *28*, 2852−2867.

https://doi.org/10.1021/acs.jpcc.4c02098
J. Phys. Chem. C 2024, 128, 14158−14167